Figure 1: Location of the shallow seismic wells, the injection well (H18A) and the monitoring well (H18B).

Figure 2: Drilling of a shallow seismic well.

Figure 3: the heat exchanger

Figure 4: pump skid during commissioning.

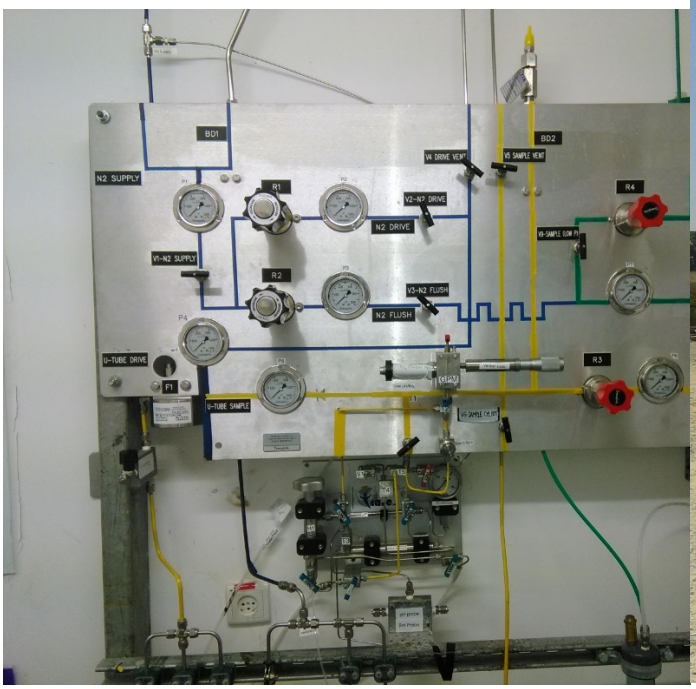

Figure 5: Utube sample lifting control panel.

Figure 6: Connection to the injection well.

Figure 7: Transfer line for the measurement of the partial pressure of the CO_2 and the pH of the water in the high pressure sample.

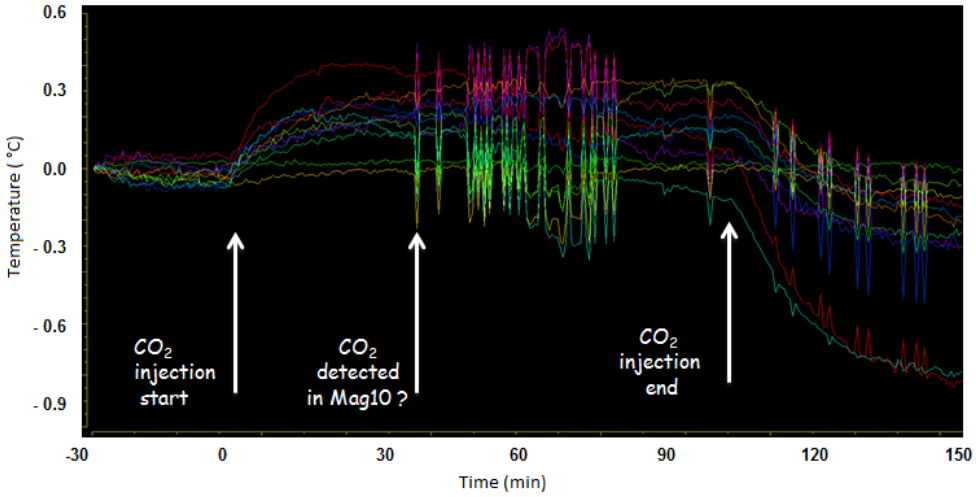

Figure 8: Downhole temperature monitoring from optical fibre using 12 Bragg's sensors.

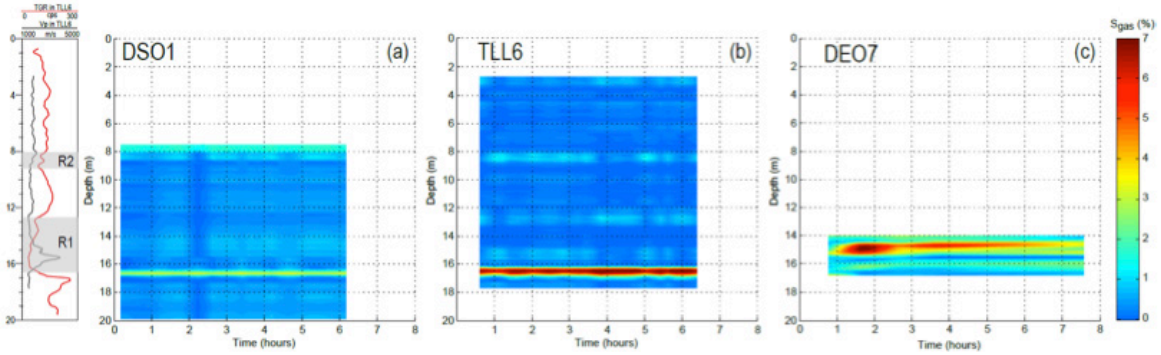

Figure 9: Biogenic gas saturation measurements at the Maguelone site from time-lapse induction logging in the DSO1 (a), TLL6 (b) boreholes, and permanent SMD electrical observatory DEO7 (c). Downhole measurements of natural gamma radioactivity (in red) and compressional acoustic velocity (in black) are provided to the left as a depth reference and for clays and sand-rich levels identification.

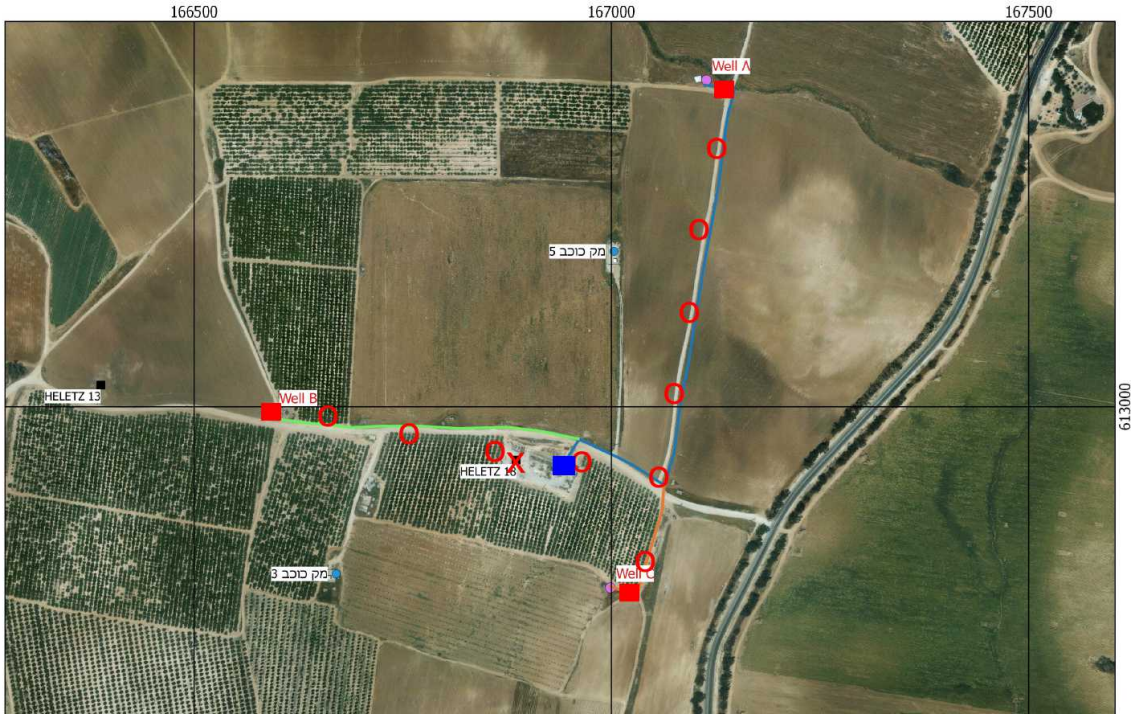

Figure 10: Planned layout of instrumentation deployment for near surface seismic.

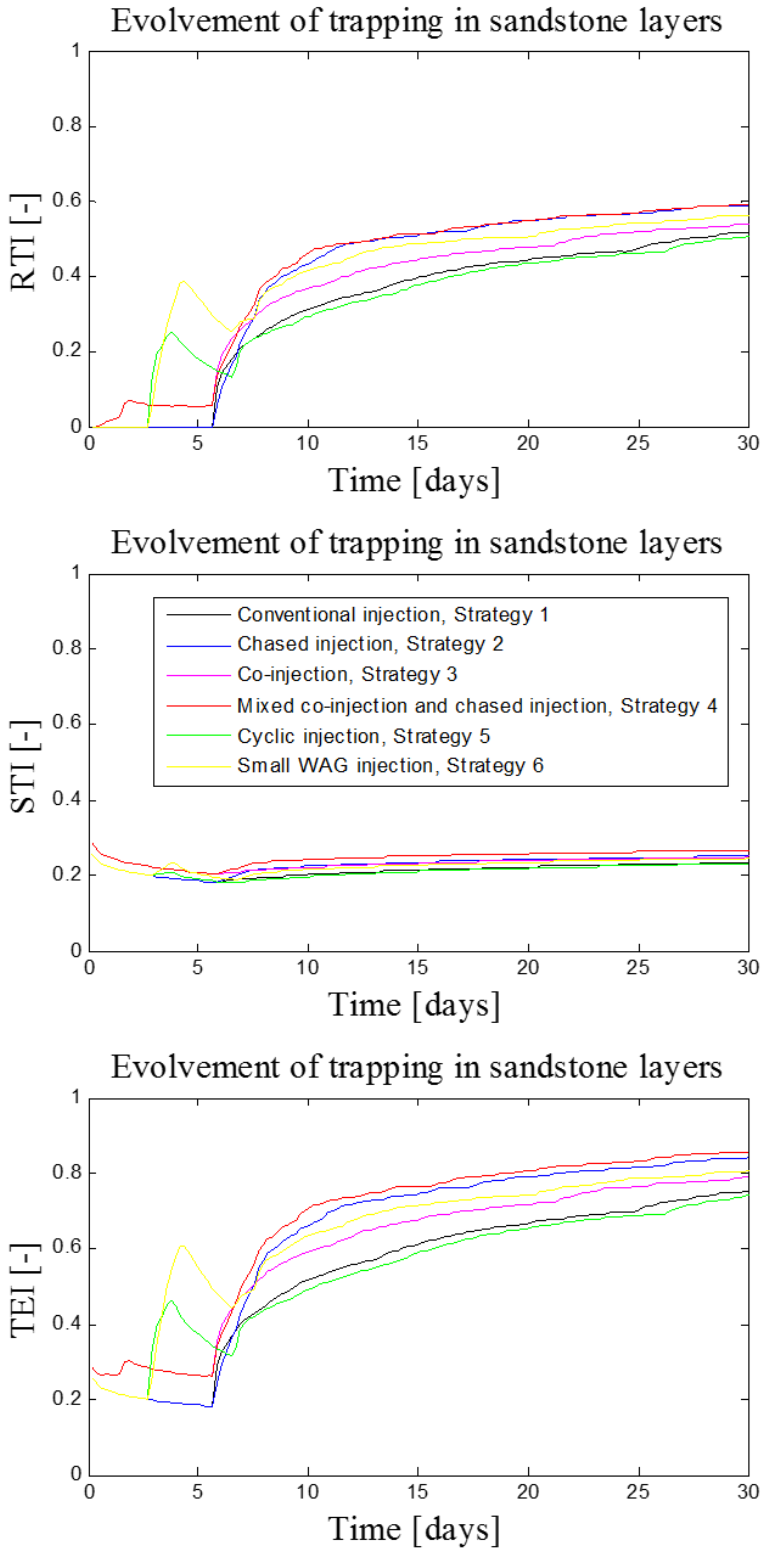

Figure 11: Evolution of residual (uppermost panel), dissolution (middle panel) and total trapping index (lower panel) for the different injection strategies identified in the Table

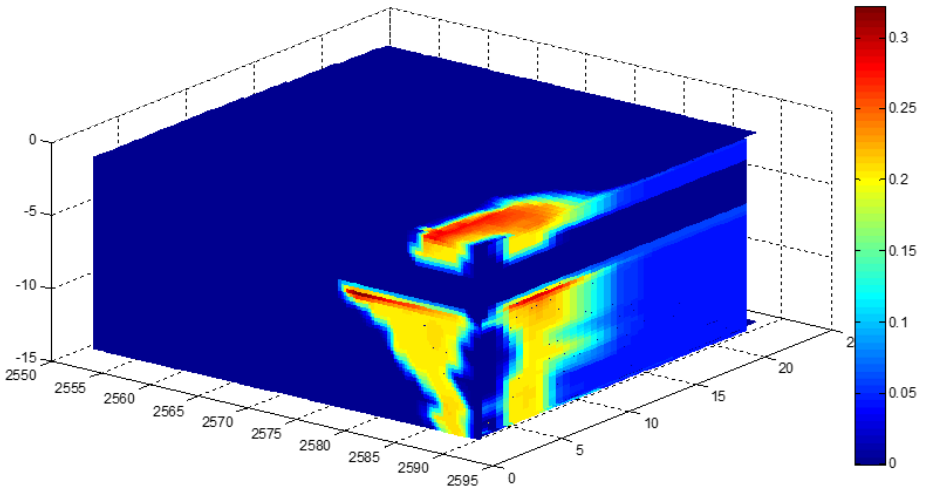

Figure12: Example of 3D heterogeneous case simulation: gas saturation after 10 days for the scenario of two cycles injection (one day gas injection following by one day water injection repeatedly with total injection rate of 2 ton/hour).

Simulations of long-term injection strategies (different injection temperature, alternating injection temperature periods) have been performed using PFLOTRAN on 10km×6km×50m 3D domain during 5-20 years. Results show that there is almost no difference in the time dependence of the near-well pressure curves between the two temperature values. On the other hand the highest injection temperature entails the largest saturation area compared with alternating injection temperature periods and the lower constant temperature injection mode. Further simulations are under way in order to examine the efficiency of alternating CO_2/brine injection periods.

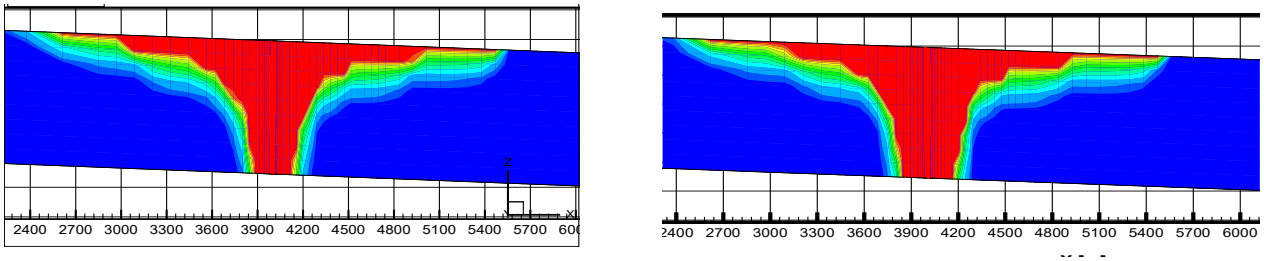

Figure13: a. Effect of intermittent mode. b. Effect of lower temperature

Figure 3.3.5: Pressure along well

Figure 3.3.6: CO_2 saturation along well

Figure 14: Pressure and CO2 saturation in the well.

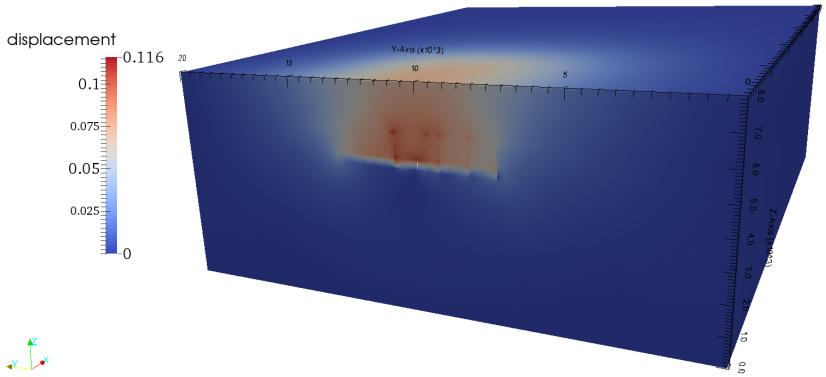

Figure 15: Field-scale validation using North Sea Goldeneye field data and measured subsidence data.

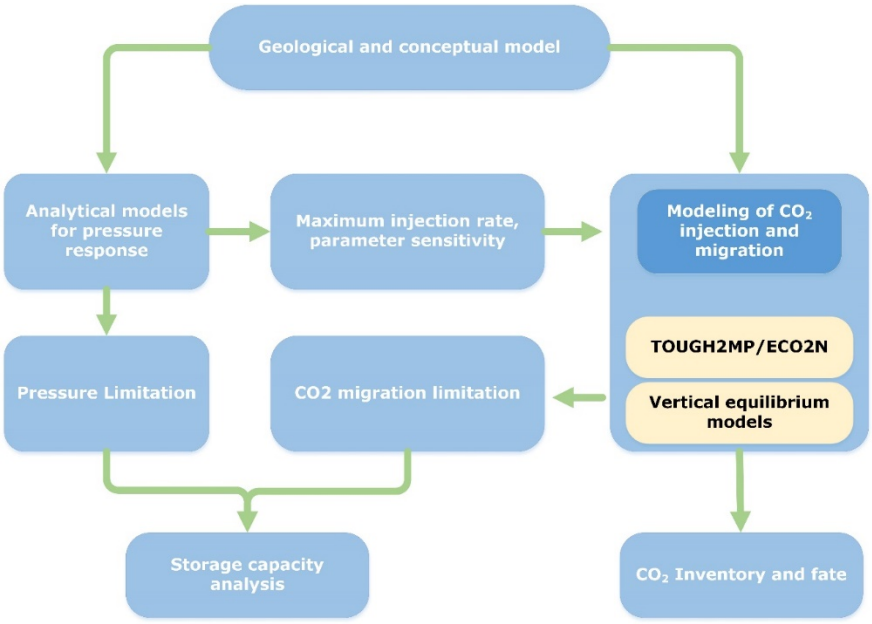

Figure 16: Basin-scale storage capacity estimation workflow.

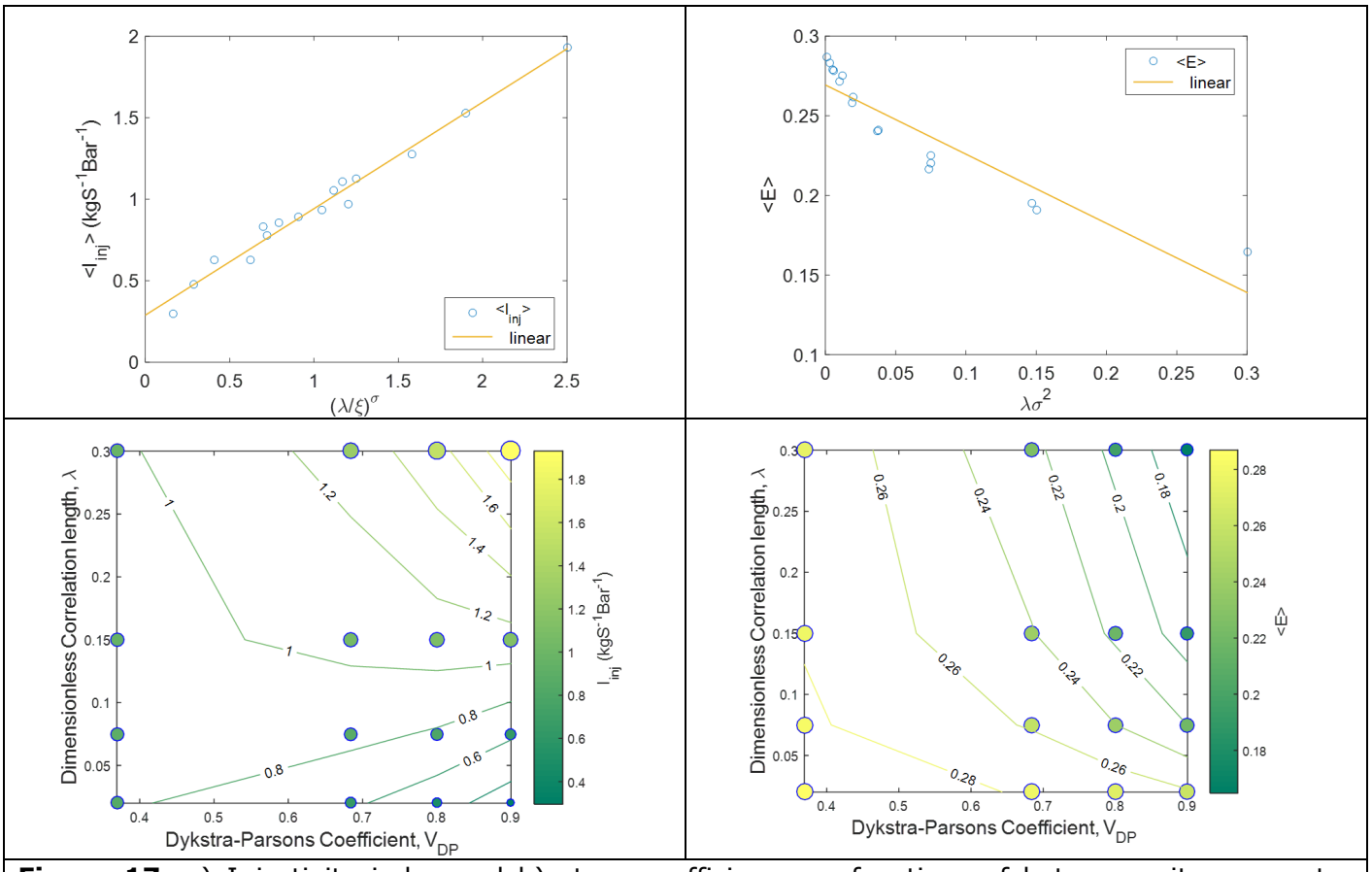

Figure 17: a) Injectivity index and b) storage efficiency as functions of heterogeneity parameter groups, where ξ is a fitting parameter, and c) injectivity index and d) strage efficiency as functions of dimensionless correlation length and Dykstra Parsons coefficient (Tian et al, 2015)

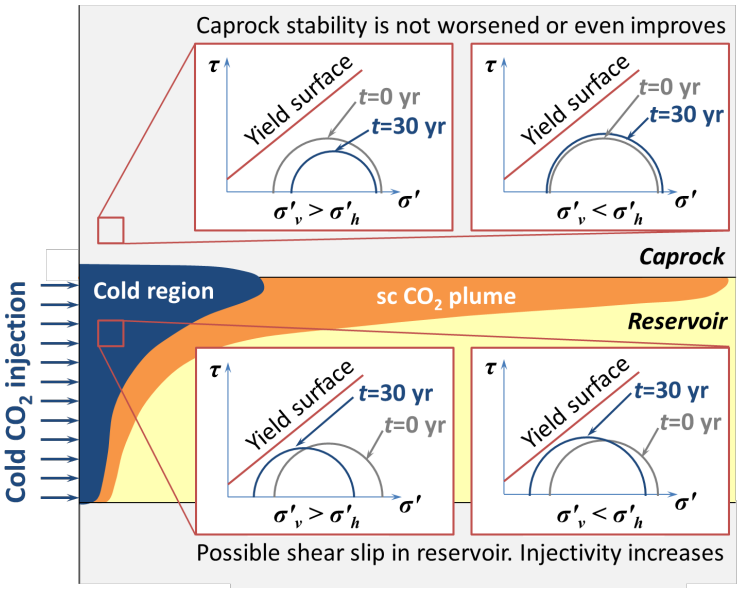

Figure 18: Sum up of the reservoir shear and caprock stability during cold CO_2 injection.

By contrast, fluid pressure becomes larger than that of a vertical well for a common length of horizontal wells (around 2 km) (see figure 3.4.3), which causes a significant increase in horizontal total stresses that improves the reservoir and caprock mechanical stability in a NF stress regime, but worsens it in a RF stress regime Though in general the caprock mechanical stability is unlikely to be compromised, fluid pressure evolution should be always monitored and mitigation measures should be carried out if it deviates from its expected evolution.

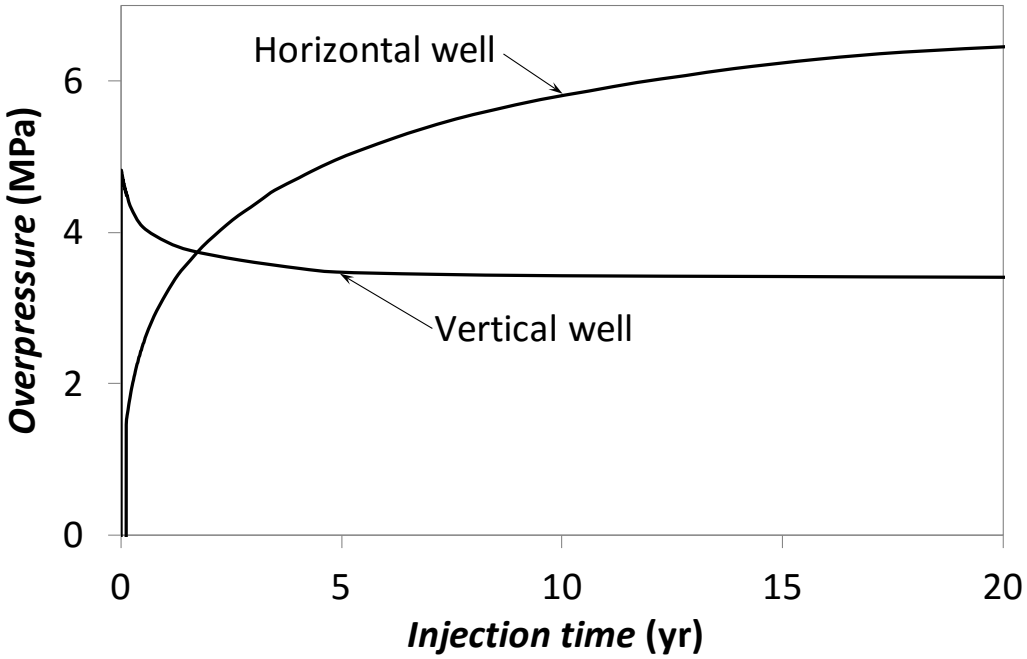

Figure 19: Overpressure evolution at the top of the aquifer next to the injection well casing when injecting CO_2 through a vertical and a horizontal well at a constant mass flow rate.

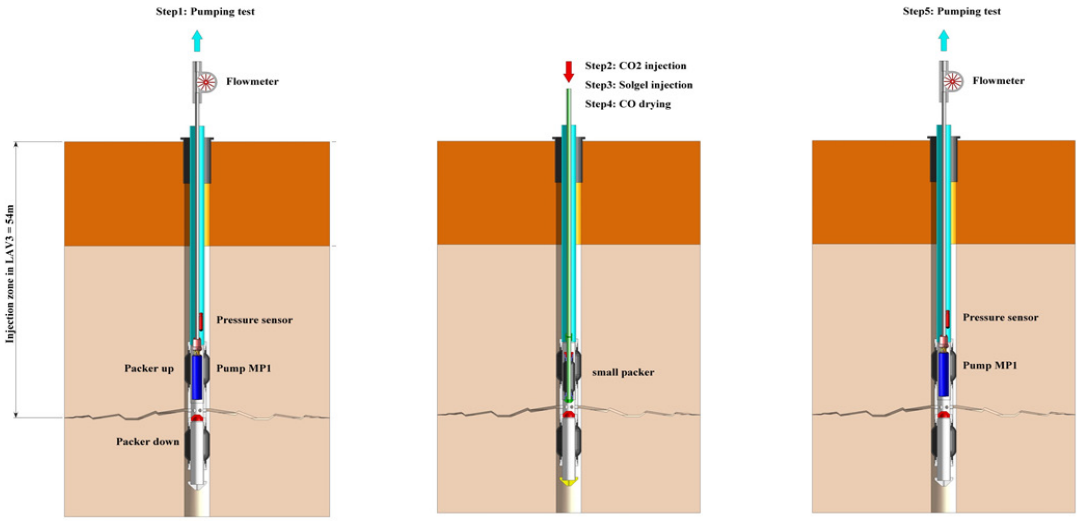

Figure 20: sketch of thee experimental protocol for the injection at CELL site.

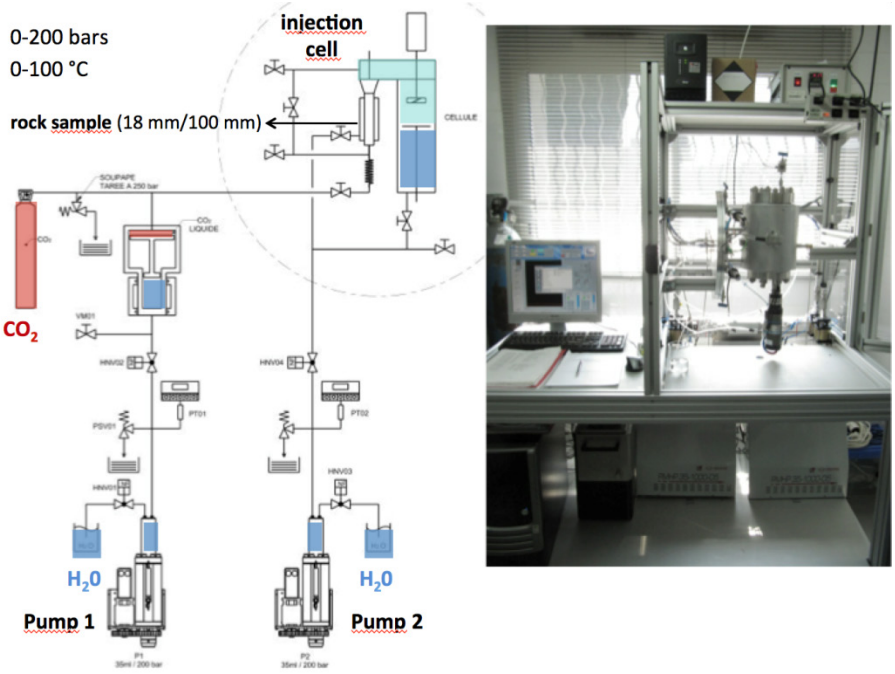

Figure 21: Diagram (left) and photograph (right) of the experimental bench ICARE 5 for carbonation experiments (reactive mineral slurry)

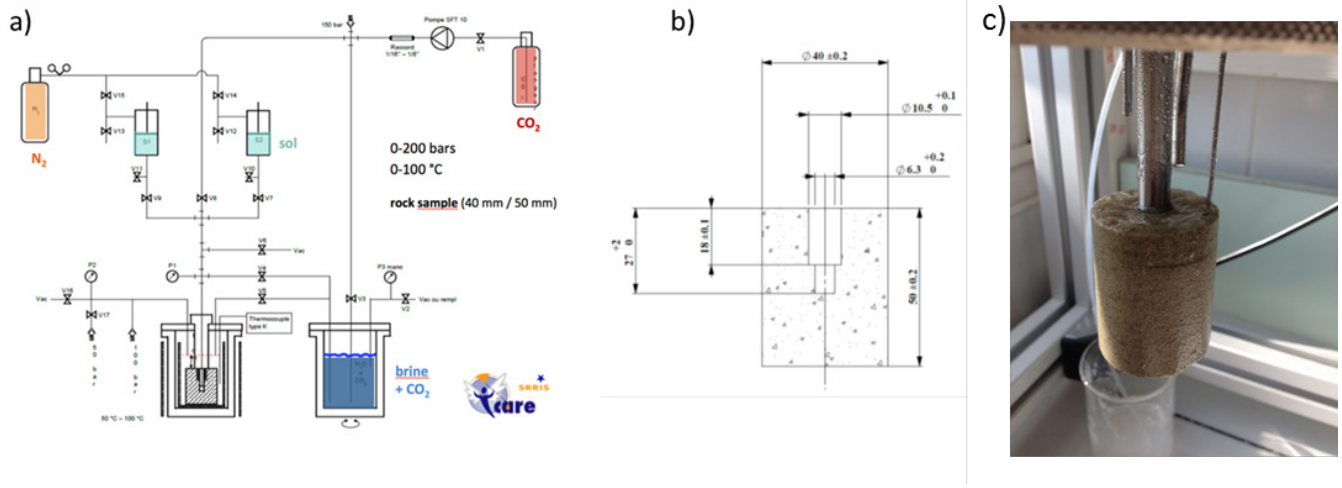

Figure 22: (a) Scale Radial Injection Simulator (SRRIS), **(b)** Sample dimensions **(c)** sample equipped with the injection tube after in injection experiment.

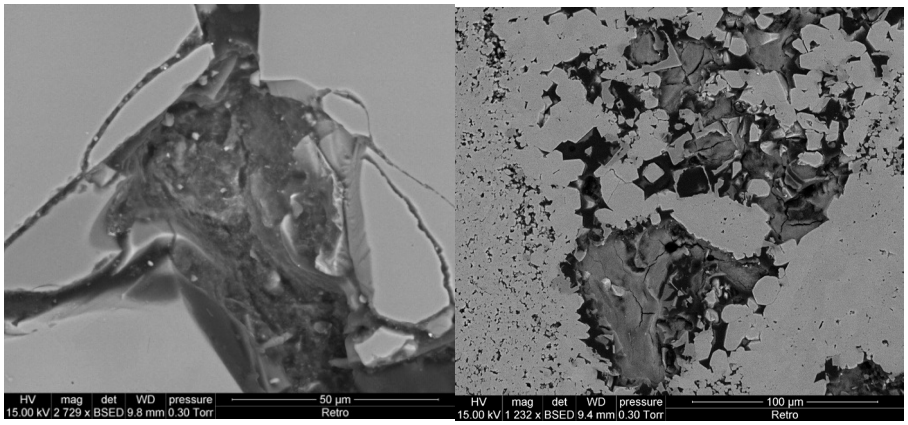

Figure 23: Solidified silica gel in Fontainebleau sandstone (left) and limestone (right).

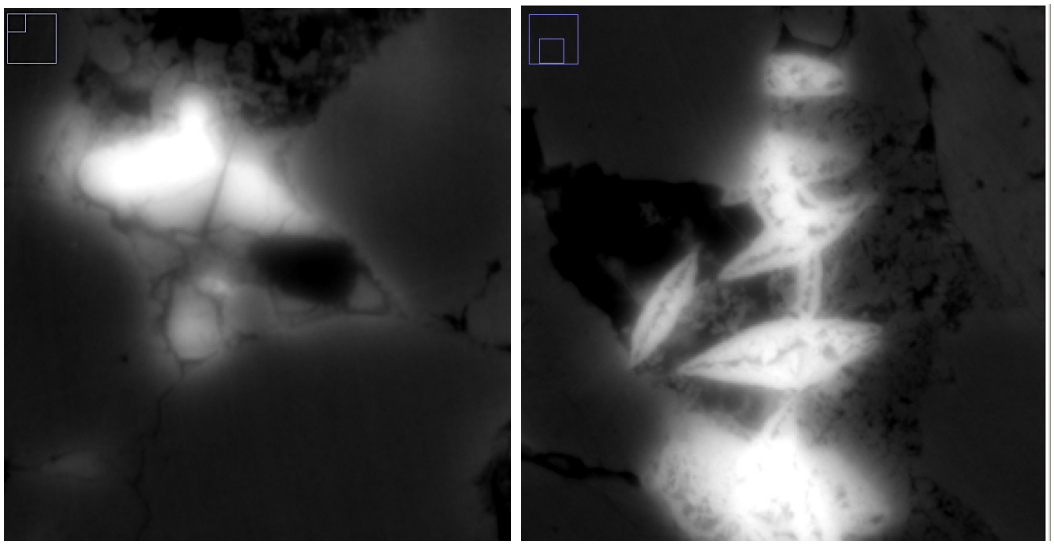

Figure 24: Cross-section of 3D X-ray micro-tomogaphy image of Berea sandstone with partial filling of the pore space by the solgel (white color) that was doped with an X-ray absorbent component (tantalum).

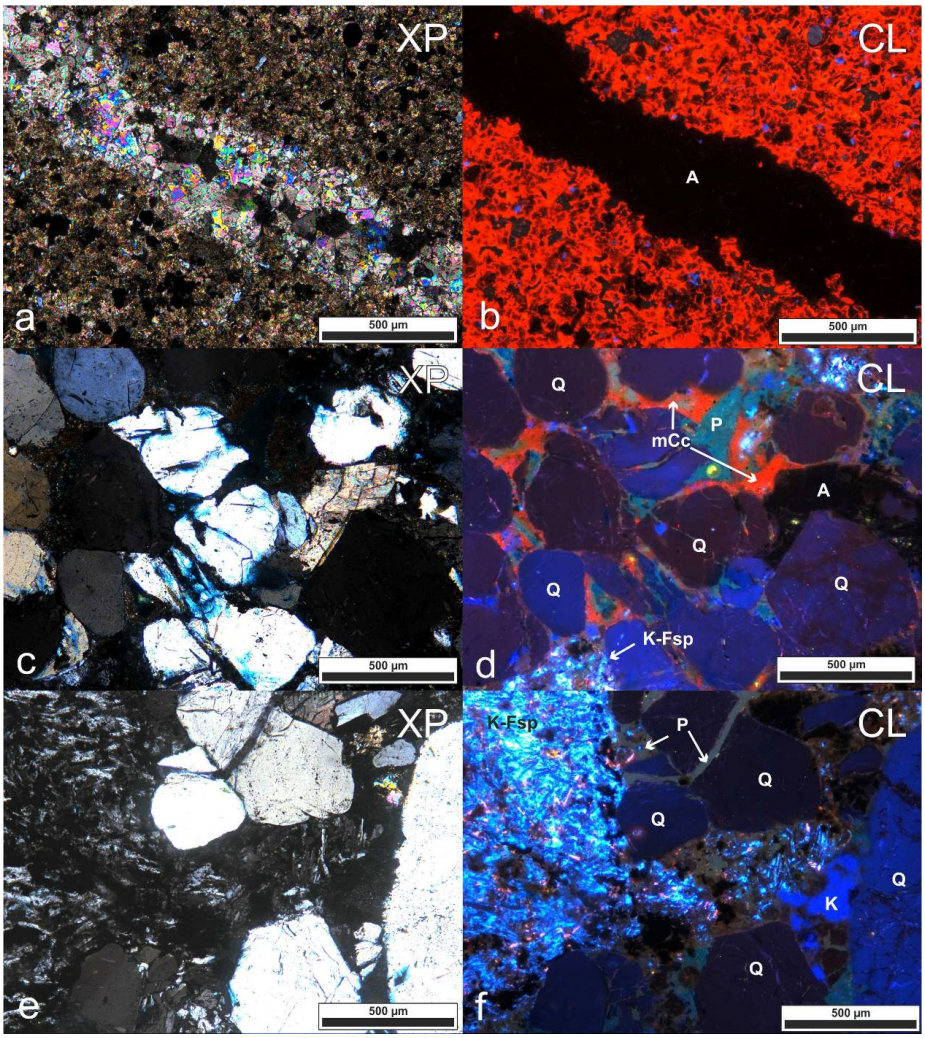

Figure 25: Representative photomicrographs of investigated rock samples in both crossed polarized light (XP) and cathodoluminescence imaging (CL). **a/b**: limestone (caprock) with calcite matrix (red) and detrital quartz (non-luminescent) and K-feldspar grains (blue); **c/d:** fine grained sandstone (f1) with micritic calcite cement (red to orange) and a single euhedral ankerite crystal (non-luminescent); **e/f**: coarse grained sandstone (g1) with kaolinite cement (dark blue) and illite cement (dark brown rims), calcite cement is missing. The grain to the left mostly consisting of bright blue luminescing potassium-feldspar is a volcanic lithoclast, the syenitic-trachytic texture is best noticeable in the XP image. A=sparitic Ankerite (cement), Q=detrital quartz grain, K-Fsp=potassium-feldspar, mCc=micritic Calcite cement, P=pore space.

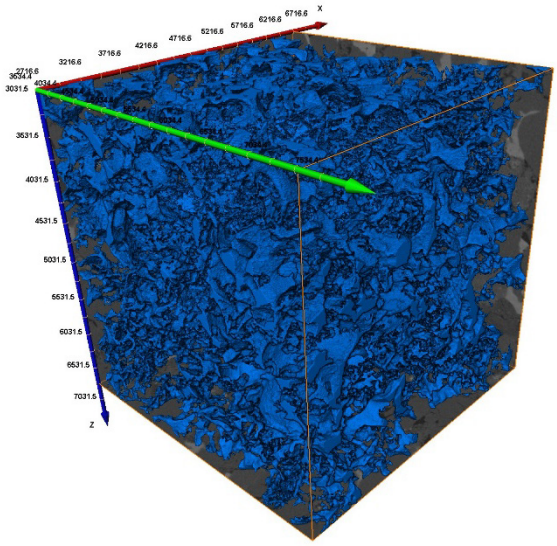

a) f1

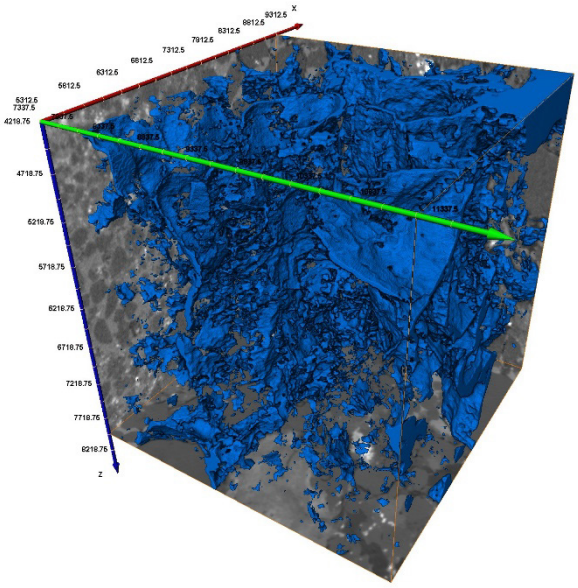

b) g1

Figure 26: Visualization of the different types of pore connectivities for the fine grained (left hand side) and coarse grained (right hand side) Heletz sandstone that have been used as for permeability tensor modeling based on μCT scans.

orm.